

however, the additional negative feedback allows exit from competence to occur at higher ComS and Rok concentrations, reducing the sensitivity of τ_{comp} to stochastic fluctuations (fig. S10).

It is not known whether competence initiation is controlled by noise, as in the model. To test the impact of noise on competence initiation, we set out to globally modulate the amount of noise in the cell. We used a *B. subtilis* strain in which the *ftsW* gene, which is necessary for septation, was replaced by an inducible copy. In the absence of inducer, septation was inhibited, resulting in elongated filamentous cells. Each filament was composed of multiple cell units, all sharing cytoplasm. Within a filament, diffusion is expected to effectively average cell contents, reducing noise in gene expression, without affecting mean concentrations of cellular components (Fig. 4A) (17). In some bacterial mutants that have elongated filamentous morphologies, cellular growth, nucleoid density, protein expression, and other physiological characteristics appear normal, even though cellular volume is greatly increased (fig. S12) (18–20). We integrated an inducible $P_{\text{hyp}}\text{-yfp}$ construct and measured the effect of cell length on cell-cell fluctuations in yellow fluorescent protein (YFP) expression (Fig. 4B). We found that noise does indeed decrease with increasing length (Fig. 4B, inset). A simple model of transcription and translation (21–24) that incorporates the continuity of filamentous cell growth produced qualitatively similar results (Fig. 4B, inset, and SOM text). Thus, cell size can in this case be used to modulate gene expression noise.

How does noise affect the probability of initiation of competence? To answer this question, we induced filamentation in the conditional *ftsW* strain at the beginning of, or before, movie acquisition and quantified P_{init} as a function of cell length. We determined length distributions of cells at the moment they initiated competence, as detected by P_{comG} expression (Fig. 4C). As a comparison, we also measured length distributions for noncompetent cells at a similar distribution of times. We plotted the relative fraction of cells that initiated competence at a given length, compared with the total number of cells at that length. The results showed that P_{init} decreased as cells elongated (Fig. 4D and SOM text). A similar decrease in P_{init} was observed in corresponding simulations (Fig. 4D). To test if the reduction in P_{init} could be due to factors other than diminished noise, we examined two promoters, P_{comS} and P_{spo0A} , both strongly regulated under these conditions. Spo0A is a master regulator of sporulation, a competing starvation response, and high concentrations of Spo0A inhibit competence (3). Conversely, P_{comS} expression is necessary for competence. Mean expression of both P_{comS} and P_{spo0A} was unaffected by cell length (fig. S17). This supports the idea that gene expression levels are independent of cell length under these conditions and that P_{init} depends on noise.

Noise may play at least three different functional roles in competence. First, noise could be

responsible for the observed variability in duration. Second, noise may be necessary to maintain excitability over a wide parameter range, by inducing escape from states of high ComK concentration. Third, noise appears to have a pivotal role in competence initiation (Fig. 4D) and thus should be considered alongside genetic parameters and circuit architecture to comprehensively understand differentiation at the single-cell level.

Quantitative analysis of a genetic system beyond its normal operating regime, including gene expression strengths, circuit architecture, and noise levels, strongly constrains dynamical models. The competence regulation system maintains excitable behavior over a broad range of parameter values. Experimentally, α_K and α_S enable P_{init} and τ_{comp} to be tuned independently, allowing the system, in theory, to adapt to independent selective pressures during evolution. The circuit can also access different dynamic regimes, such as oscillation and bistability, indicating its potential to evolve alternative qualitative behaviors.

References and Notes

- U. Alon, *An Introduction to Systems Biology: Design Principles of Biological Circuits*. Mathematical and Computational Biology Series, vol. 10 (Chapman & Hall/CRC, Boca Raton, FL, 2006).
- D. Dubnau, *Annu. Rev. Microbiol.* **53**, 217 (1999).
- A. D. Grossman, *Annu. Rev. Genet.* **29**, 477 (1995).
- G. M. Suel et al., *Nature* **440**, 545 (2006).
- R. M. Berka et al., *Mol. Microbiol.* **43**, 1331 (2002).
- D. van Sinderen et al., *Mol. Microbiol.* **15**, 455 (1995).
- H. Maamar, D. Dubnau, *Mol. Microbiol.* **56**, 615 (2005).
- W. K. Smits et al., *Mol. Microbiol.* **56**, 604 (2005).
- K. Turgay et al., *EMBO J.* **17**, 6730 (1998).
- J. Hahn, L. Kong, D. Dubnau, *J. Bacteriol.* **176**, 5753 (1994).
- M. Ogura et al., *Mol. Microbiol.* **32**, 799 (1999).
- C. Koch, *Biophysics of Computation* (Oxford Univ. Press, Oxford, 1999).
- D. Dubnau, R. Losick, *Mol. Microbiol.* **61**, 564 (2006).
- D. T. Gillespie, *J. Phys. Chem.* **81**, 2340 (1977).
- The gene circuit shown in Fig. 1B can be described, in a continuous approximation, by two coupled differential equations that govern the dynamical evolution of the

concentrations of ComK and ComS proteins, denoted K and S, respectively. The equation for K is $\frac{dK}{dt} = \alpha_K + \frac{\beta_K K^n}{K^n + K^n + 1 + K/I_K + S/I_S} - \lambda_K K$, where α_K and β_K parameterize the strength of constitutive and autoregulated ComK expression, respectively. The third term models degradation through competitive binding of ComK and ComS to MecA. The final term represents linear degradation of ComK. The equation for S is $\frac{dS}{dt} = \alpha_S + \frac{\beta_S}{1 + (K/I_K)^n + 1 + K/I_K + S/I_S} - \lambda_S S$. Here, α_S and β_S measure the strength of constitutive and regulated *comS* expression, respectively. The third and fourth terms represent MecA-mediated and linear degradation, respectively. Other parameters are defined in the SOM text. We have also developed a discrete model of the circuit that incorporates intrinsic noise explicitly. The requirement of independent tunability of P_{init} and τ_{comp} strongly constrains the allowed parameter values and thus the structure of the phase space. The modeling is described in detail in the SOM text.

- T. T. Hoa et al., *Mol. Microbiol.* **43**, 15 (2002).
- M. B. Elowitz et al., *J. Bacteriol.* **181**, 197 (1999).
- F. Ishino et al., *J. Bacteriol.* **171**, 5523 (1989).
- N. Maki et al., *J. Bacteriol.* **182**, 4337 (2000).
- F. Tetart et al., *Mol. Microbiol.* **6**, 621 (1992).
- H. H. McAdams, A. Arkin, *Proc. Natl. Acad. Sci. U.S.A.* **94**, 814 (1997).
- J. Paulsson, *Nature* **427**, 415 (2004).
- P. S. Swain, M. B. Elowitz, E. D. Siggia, *Proc. Natl. Acad. Sci. U.S.A.* **99**, 12795 (2002).
- M. Thattai, A. van Oudenaarden, *Proc. Natl. Acad. Sci. U.S.A.* **98**, 8614 (2001).
- We thank R. Kishony, B. Shraiman, U. Alon, R. Ranganathan, S. Altschuler, L. Wu, and K. Süel, together with members of the Elowitz laboratory, for thoughtful comments and discussions. This work was supported by grants from NIH (R01 GM079771 to M.B.E. and GM068763 to the Center for Modular Biology), the Searle Scholars Program, the Human Frontiers Science Program, and the Packard Foundation. G.M.S. is supported by California Institute of Technology Center for Biological Circuit Design and the University of Texas Southwestern's Endowed Scholars Program. J.G.O. acknowledges financial support from the Ministerio de Educación y Ciencia (Spain, project FIS2006-11452) and from the Generalitat de Catalunya.

Supporting Online Material

www.sciencemag.org/cgi/content/full/315/5819/1716/DC1
Materials and Methods

SOM Text

Figs. S1 to S17

Tables S1 to S4

References

13 November 2006; accepted 26 February 2007
10.1126/science.1137455

Temporal Frequency of Subthreshold Oscillations Scales with Entorhinal Grid Cell Field Spacing

Lisa M. Giocomo,^{1*} Eric A. Zilli,¹ Erik Fransén,² Michael E. Hasselmo^{1*}

Grid cells in layer II of rat entorhinal cortex fire to spatial locations in a repeating hexagonal grid, with smaller spacing between grid fields for neurons in more dorsal anatomical locations. Data from in vitro whole-cell patch recordings showed differences in frequency of subthreshold membrane potential oscillations in entorhinal neurons that correspond to different positions along the dorsal-to-ventral axis, supporting a model of physiological mechanisms for grid cell responses.

The entorhinal cortex plays an important role in encoding of spatial information (1–3) and episodic memory (4). Many layer II neurons of rat entorhinal cortex are grid cells, firing when the rat is in an array of spatial locations forming a hexagonal grid within the environment

(5–7). The spacing of firing fields in the grid varies with anatomical position of the cell along the dorsal-ventral axis of entorhinal cortex, as measured by distance from the posthinal border (5). Neurons closer to the dorsal border of entorhinal cortex have shorter distances between firing fields. Computa-

tional models explicitly predict that differences in grid field spacing should correspond to differences in intrinsic frequencies of neurons along the dorsal-to-ventral axis (3, 8). This could provide systematic variation in the gain of a movement-speed signal for path integration (2, 3, 9).

Subthreshold membrane potential oscillations in entorhinal cortical stellate cells (10) arise from a single-cell mechanism involving voltage-sensitive currents (11–13) and could contribute to network

dynamics (14). We recorded subthreshold oscillations from 57 stellate cells in layer II of medial entorhinal cortex (fig. S1) in slices from different anatomical positions along the dorsal-ventral axis by using whole-cell patch clamp techniques (15). The position of each horizontal slice was measured individually relative to the dorsal surface of the brain (Fig. 1A).

Stellate cells in dorsal entorhinal cortex showed higher temporal frequencies (f) of subthreshold membrane potential oscillations compared with lower frequencies in cells from more ventral entorhinal slices (Fig. 1B). Dorsal cells ($n = 30$) were defined as cells recorded in slices taken between 3.8 mm [the border with postsubiculum (16)] and 4.9 mm from the dorsal surface of the brain. Ventral cells ($n = 27$) were defined as

cells recorded in slices between 4.9 and 7.1 mm from the dorsal surface. Because the group means of the frequency of subthreshold oscillations recorded from these populations (Fig. 1B) can depend upon the mean membrane potential voltage, we performed this analysis separately for data gathered at different approximate holding membrane potentials of -50 mV and -45 mV. The mean frequency in dorsal cells was significantly higher than the mean frequency in ventral cells for measurements at about -50 mV (dorsal mean $f \pm \text{SEM} = 6.42 \pm 0.40$ Hz and $n = 28$; ventral $f = 4.23 \pm 0.32$ Hz and $n = 25$; $P < 0.001$) and -45 mV (dorsal mean $f \pm \text{SEM} = 7.18 \pm 0.50$ Hz and $n = 14$; ventral $f = 4.88 \pm 0.59$ Hz and $n = 7$; $P < 0.01$). Frequencies were determined by an automated autocorrelation anal-

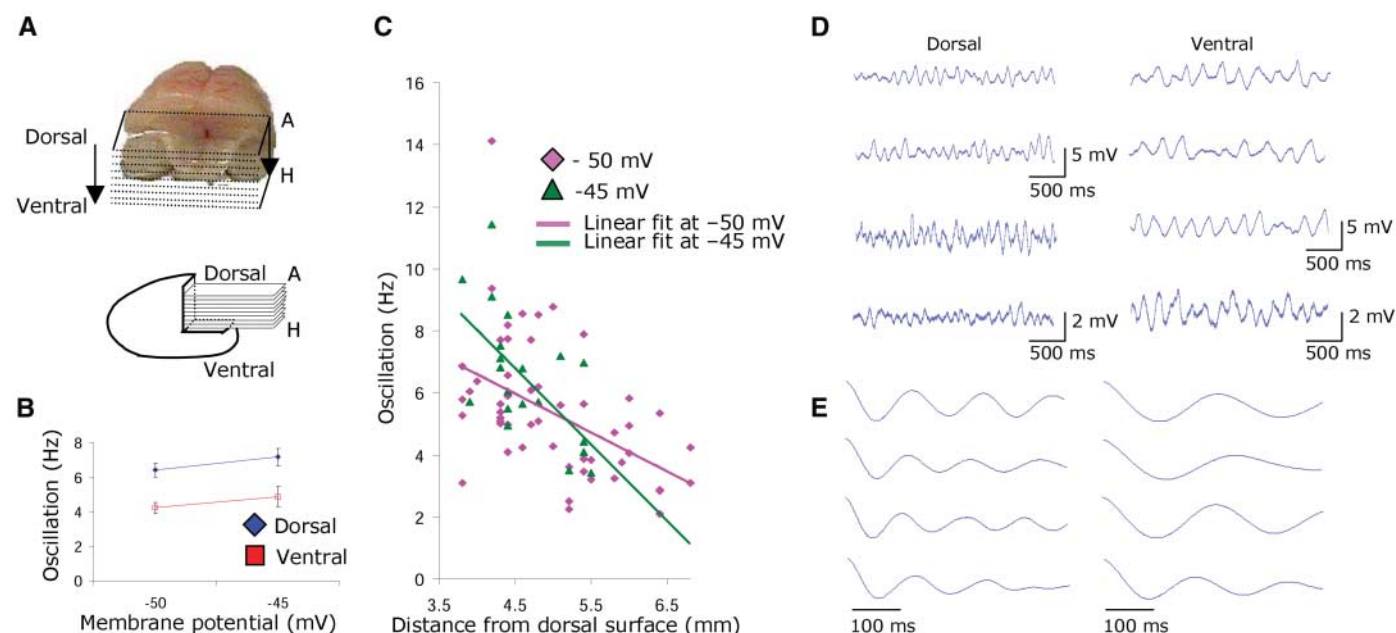


Fig. 1. Higher frequency of subthreshold oscillations in dorsal versus ventral entorhinal cortex. **(A)** Top, dorsal view of brain after slicing. Bottom, sagittal view showing anatomical location of horizontal slices A to H. **(B)** Mean frequency of subthreshold oscillations for neurons from dorsal slices (3.8 to 4.9 mm bregma) and ventral slices (4.9 to 7.1 mm bregma) at -50 mV and

-45 mV. Error bars indicate SEM. **(C)** Subthreshold oscillation frequency plotted versus anatomical distance from dorsal surface. **(D)** Examples of subthreshold oscillations at -50 mV in dorsal regions (left) and ventral regions (right). **(E)** Corresponding autocorrelations used to measure frequency in (D).

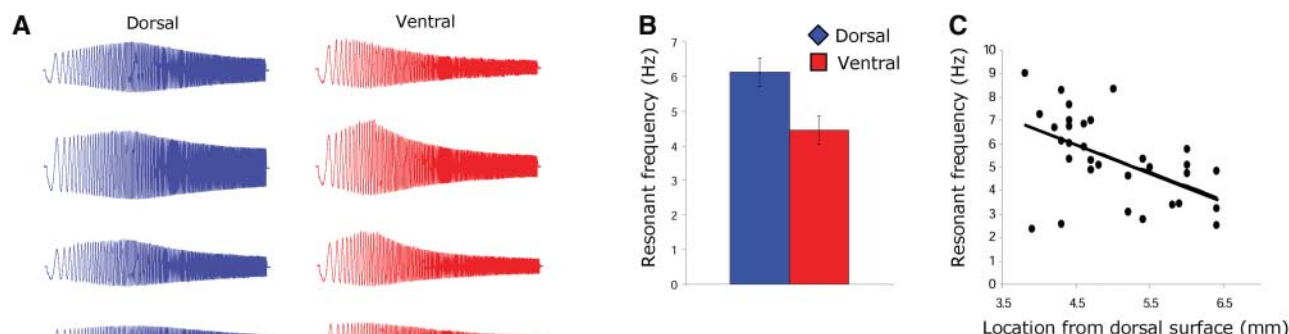


Fig. 2. Differences in resonance properties of neurons in dorsal versus ventral entorhinal cortex. **(A)** Examples of resonance responses of neurons in dorsal (blue) and ventral (red) entorhinal cortex (black) in response to ZAP stimulus. **(B)** Histogram of mean peak resonance frequency for neurons in dorsal versus ventral entorhinal cortex. **(C)** Resonance frequency plotted versus anatomical distance from the dorsal surface.

ysis algorithm (15) and were used throughout unless otherwise noted. The significant difference between mean frequencies was replicated with analyses using the peak in the power spectra for data at -50 mV (dorsal $f = 4.86 \pm 0.37$ Hz and $n = 28$; ventral $f = 3.44 \pm 0.25$ Hz and $n = 25$; $P < 0.01$) and -45 mV (dorsal $f = 5.54 \pm 0.49$ Hz and $n = 14$; ventral $f = 3.76 \pm 0.31$ Hz and $n = 8$; $P < 0.01$) (fig. S2). The resting membrane potential, firing threshold, resistance, and age [dorsal mean age \pm SEM = 19.8 ± 0.4 days and ventral age = 19.1 ± 0.4 days, P value not significant (NS)] did not contribute to the difference in the frequency of oscillations observed between neurons from dorsal versus ventral slices (15).

Entorhinal neurons showed a systematic difference in subthreshold oscillation frequency when plotted for different locations along the dorsal-ventral axis (Fig. 1C) for data at -50 mV ($r = 0.48$, slope = -1.26) and at -45 mV ($r = 0.60$, slope =

-2.48). This pattern resembles the difference in spatial periodicity of grid cells previously recorded from layer II at different positions along the dorsal-ventral-axis in awake, behaving animals (5, 7). Examples of subthreshold oscillations recorded from individual entorhinal neurons illustrate the difference in dorsal versus ventral frequency (Fig. 1D). 500-ms segments of the autocorrelations computed for the same cells in Fig. 1D demonstrate the difference in peak-to-peak wavelength (Fig. 1E).

The frequency of subthreshold oscillations has been shown to correlate with the peak frequency of membrane potential resonance at rest (-60 to -64 mV) in entorhinal neurons (17). We evaluated the resonant frequency of neurons by delivering a 20-s-long impedance amplitude profile (ZAP) stimulus and measuring the input frequency that caused the largest amplitude depolarization of membrane potential. Individual examples of the response to the ZAP stimulus are shown for four

neurons from dorsal entorhinal slices (Fig. 2A) and four neurons from more-ventral slices. The resonant frequency of stellate cells was significantly higher in dorsal cells compared with that in ventral cells (dorsal frequency = 6.13 ± 0.41 Hz and $n = 18$; ventral frequency = 4.45 ± 0.40 Hz and $n = 14$; $P < 0.01$) (Fig. 2B). There was no significant difference in resting potential between the populations used for this analysis (dorsal potential = -60.12 ± 0.26 mV and $n = 18$; ventral potential = -60.11 ± 0.26 mV and $n = 14$; P NS). Resonant frequency was systematically higher in dorsal regions when plotted in relation to anatomical location ($r = 0.51$, slope = -1.18) (Fig. 2C).

To analyze the relationship of subthreshold oscillations to other intrinsic properties, we measured the change in membrane potential during a hyperpolarizing current injection that usually caused a slow depolarizing shift (a "sag" of the membrane potential). The sag was fit with a dual exponential equation starting just after the trough of the sag and ending near the end of the current injection at steady state potential (Fig. 3, A and B). The faster of the two time constants (τ_1) of the sag was measured for hyperpolarizing current steps that ended at steady-state membrane voltages of -69.9 to -65 mV (V1) and at steady-state membrane voltages of -64.9 to -60 mV (V2). The time constant (τ_1) of the sag increased with depth on the dorsal-ventral axis (at V1, $r = 0.55$ and slope = 9.67 ; at V2, $r = 0.61$ and slope = 8.23) (Fig. 3C), with significantly faster values of τ_1 in more-dorsal portions compared with more-ventral portions at V1 (dorsal $\tau_1 = 23.37 \pm 1.24$ ms and $n = 17$; ventral $\tau_1 = 35.52 \pm 1.81$ ms, $n = 14$; $P < 0.01$) and at V2 (dorsal $\tau_1 = 22.37 \pm 1.60$ ms and $n = 11$; ventral $\tau_1 = 34.71 \pm 2.68$ ms and $n = 17$; $P < 0.01$). The τ_1 of the sag correlated with the frequency of subthreshold oscillations (at V1, $r = 0.63$ and slope = -4.32 ; at V2, $r = 0.65$ and slope = -4.10) (Fig. 3D). Voltage-clamp studies are necessary to confirm underlying currents. A potential candidate is the h current, which has been shown to underlie sag in stellate cells (11, 12).

The differences in temporal frequency shown in this study correspond to differences in spatial periodicity of unit firing observed with extracellular recording in awake, behaving animals (5–7). Neurons at more-dorsal locations show higher intrinsic subthreshold oscillation frequency in vitro and smaller spacing between grid fields in vivo. Plots of the reciprocal of temporal frequency versus anatomical position (Fig. 4A) reveal slopes similar to the slope of grid field spacing (G) relative to anatomical position (Fig. 4B).

These data support the prediction of a model (SOM text) (3, 8) related to other models of grid cells and theta phase precession (18–20). In this model, grid cell periodicity arises from an interference pattern generated by intrinsic temporal oscillations in the soma and dendrites of a single cell. During simulated rat movement, cells modulated by head direction and speed (7, 21, 22) shift the frequency of dendritic oscillations (consistent with voltage effects on frequency). The grid pattern is the product of interference by three

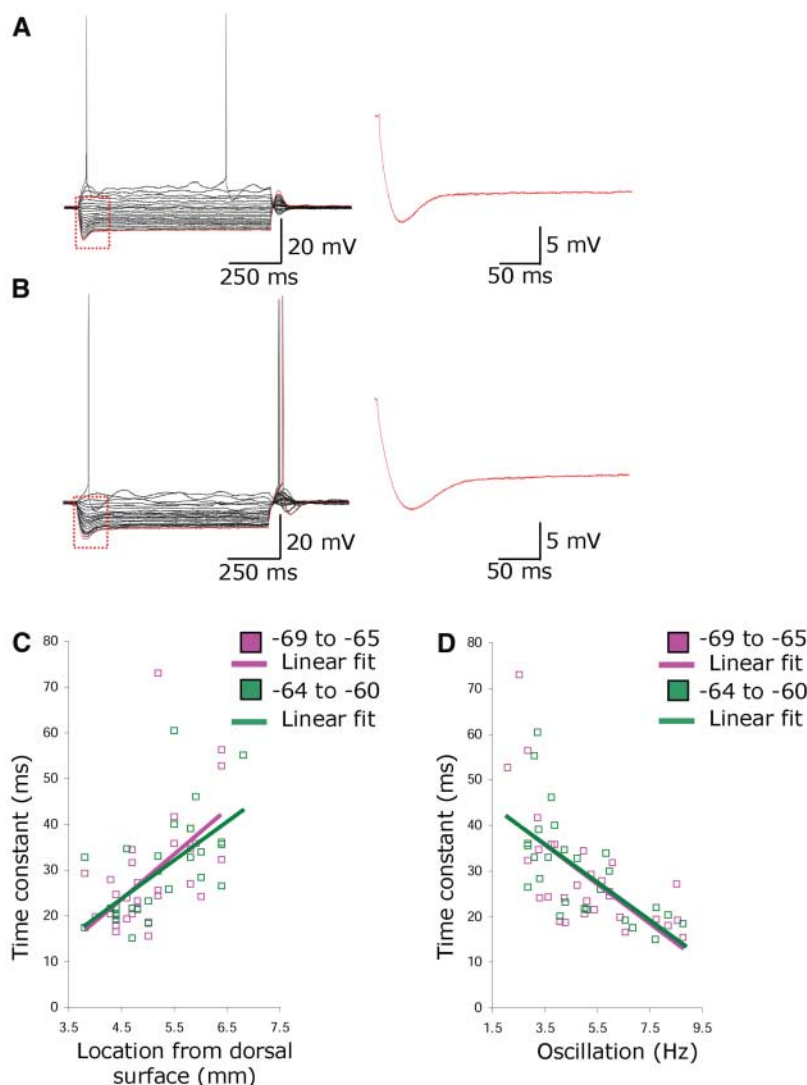


Fig. 3. Relationship of subthreshold membrane potential oscillations to sag potential. For single neurons in dorsal (A) and ventral entorhinal cortex (B), traces on left show membrane potential responses to multiple current injection levels. Single traces (right) show sag potentials at higher resolution. (C) τ_1 of sag potential (ms) plotted versus anatomical location. (D) τ_1 of sag potential plotted versus subthreshold oscillation frequency.

dendritic oscillations, each receiving a different head direction input, shifting in and out of phase with soma oscillations in proportion to distance moved in the preferred direction of each head direction cell. Spiking occurs when all three dendrites are in phase with the soma, causing oscillations to cross threshold (figs. S4 and S5). Spiking does not alter soma or dendritic phase but occurs with theta rhythmicity, consistent with *in vivo* recordings in entorhinal cortex (5–7) and hippocampus (2, 9, 18) and potentially causing precession relative to field potential oscillations (3, 8, 19, 20).

The model (3, 8) was modified to include shifts in dendritic frequency proportional to soma frequency and to use a scaling factor, $H = fG$ (fig. S6), determined from the experimental data. Simulations (SOM text) (Fig. 4, C and D) demonstrated that differences in temporal frequency of somatic oscillations result in different grid field spacing. Insertion of the experimentally determined value for subthreshold oscillation frequency (f) at a par-

ticular anatomical location resulted in simulated grid cell spacing that matches data (7) on grid cell spacing (G) at the same anatomical location (figs. S4 and S7).

The model demonstrates one possible mechanism for path integration (2) and supports the prediction that systematic variation in gain of a movement-speed signal could underlie differences in grid field spacing (2, 9). The model is compatible with maintenance of grid cell representations by persistent firing (23) or attractor dynamics arising from patterned excitatory connectivity (2, 24, 25). Long-term stability of grid fields could require place cell input dependent on external landmarks (3, 8, 26). Differences in intrinsic frequency along the dorsal-ventral axis of entorhinal cortex could contribute to differences in place field size along the septal-to-temporal axis of the hippocampus (9, 27).

The systematic differences in intrinsic temporal frequency may provide multiple scales for

coding of both space and time. Periodic representation of the environment at multiple spatial scales could prove essential to mechanisms of path integration (2, 3, 9, 28), consistent with impairments after entorhinal lesions (1). Coding of continuous dimensions by interacting frequencies could also allow the coding of continuous relative time necessary for episodic memory (29). These results suggest that, beyond simple summation of input, neural processing involves interactions of synaptic input and interference between intrinsic frequencies (8, 9, 18, 19).

References and Notes

1. H. A. Steffenach, M. Witter, M.-B. Moser, E. I. Moser, *Neuron* **45**, 301 (2005).
2. B. L. McNaughton, F. P. Battaglia, O. Jensen, E. I. Moser, M.-B. Moser, *Nat. Rev. Neurosci.* **7**, 663 (2006).
3. J. O'Keefe, N. Burgess, *Hippocampus* **15**, 853 (2005).
4. H. Eichenbaum, N. J. Cohen, *From Conditioning to Conscious Recollection* (Oxford Univ. Press, New York, 2003).
5. T. Hafting, M. Fyhn, S. Molden, M.-B. Moser, E. I. Moser, *Nature* **436**, 801 (2005).
6. M. Fyhn, S. Molden, M. P. Witter, E. I. Moser, M.-B. Moser, *Science* **305**, 1258 (2004).
7. F. Sargolini *et al.*, *Science* **312**, 758 (2006).
8. N. Burgess, C. Barry, J. O'Keefe, *Hippocampus*, in press.
9. A. P. Maurer, S. R. VanRhoode, G. R. Sutherland, P. Lipa, B. L. McNaughton, *Hippocampus* **15**, 841 (2005).
10. A. Alonso, R. R. Llinas, *Nature* **342**, 175 (1989).
11. C. T. Dickson *et al.*, *J. Neurophysiol.* **83**, 2562 (2000).
12. E. Fransen, A. A. Alonso, C. T. Dickson, J. Magistretti, M. E. Hasselmo, *Hippocampus* **14**, 368 (2004).
13. J. A. White, R. Klink, A. Alonso, A. R. Kay, *J. Neurophysiol.* **80**, 262 (1998).
14. C. D. Acker, N. Kopell, J. A. White, *J. Comput. Neurosci.* **15**, 71 (2003).
15. Materials and methods are available on Science Online.
16. G. Paxinos, C. Watson, *The Rat Brain in Stereotaxic Coordinates* (Academic Press, San Diego, CA, 1998).
17. I. Erchova, G. Kreck, U. Heinemann, A. V. Herz, *J. Physiol.* **560**, 89 (2004).
18. J. O'Keefe, M. L. Recce, *Hippocampus* **3**, 317 (1993).
19. M. Lengyel, Z. Szatmari, P. Erdi, *Hippocampus* **13**, 700 (2003).
20. H. T. Blair, A. C. Welday, K. Zhang, *J. Neurosci.*, in press.
21. J. S. Taube, J. P. Bassett, *Cereb. Cortex* **13**, 1162 (2003).
22. P. E. Sharp, H. T. Blair, J. Cho, *Trends Neurosci.* **24**, 289 (2001).
23. E. Fransén, B. Tahvildari, A. V. Egorov, M. E. Hasselmo, A. A. Alonso, *Neuron* **49**, 735 (2006).
24. M. C. Fuhs, D. S. Touretzky, *J. Neurosci.* **26**, 4266 (2006).
25. A. Samsonovich, B. L. McNaughton, *J. Neurosci.* **17**, 5900 (1997).
26. J. J. Knierim, H. S. Kudrimoti, B. L. McNaughton, *J. Neurophysiol.* **80**, 425 (1998).
27. T. Solstad, E. I. Moser, G. T. Einevoll, *Hippocampus* **16**, 1026 (2006).
28. A. D. Redish, D. S. Touretzky, *Hippocampus* **7**, 15 (1997).
29. M. E. Hasselmo, H. Eichenbaum, *Neural Netw.* **18**, 1172 (2005).
30. Thanks to E. Moser, M.-B. Moser, M. Yoshida, K. Lillis, H. Eichenbaum, and J. White for advice and comments. Research supported by National Institute of Mental Health (NIMH) grant MH60013, Silvio O. Conte Center grant NIMH MH71702, NSF Science of Learning Center SBE 0354378, and National Institute on Drug Abuse grant DA16454 (part of the Collaborative Research in Computational Neuroscience program).

Supporting Online Material

www.sciencemag.org/cgi/content/full/315/5819/1719/DC1
Materials and Methods

SOM Text
Figs. S1 to S7

22 December 2006; accepted 23 February 2007
10.1126/science.1139207

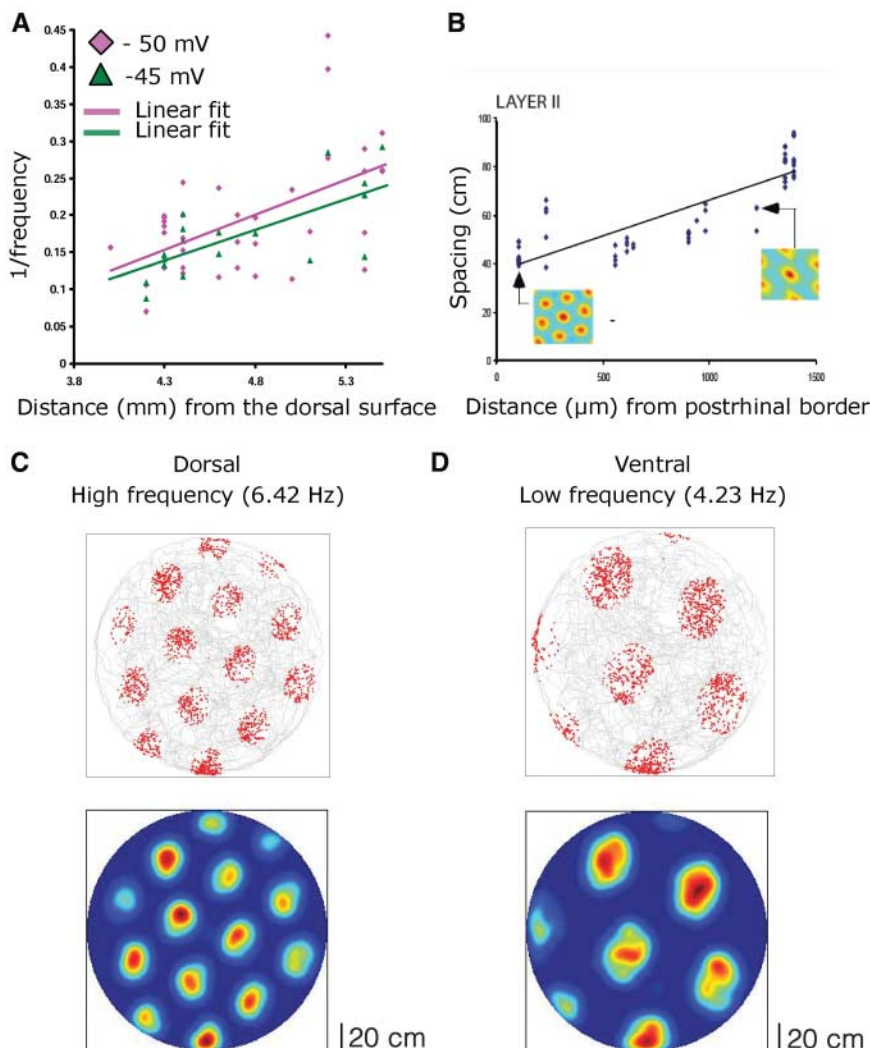


Fig. 4. Subthreshold oscillations may underlie differences in grid field spacing. (A) Reciprocal of oscillation frequency plotted versus anatomical depth for anatomical range matching a previous publication (7) as shown in (B). (C and D) Simulations of grid cell model (3, 8). Top, gray indicates trajectory of simulated rat. Red indicates firing locations. Bottom, firing rate map (red, maximum; blue, no spikes). Grid field spacing is small for mean dorsal oscillation frequency of 6.42 Hz (C) and larger for mean ventral frequency of 4.23 Hz (D).

This copy is for your personal, non-commercial use only.

If you wish to distribute this article to others, you can order high-quality copies for your colleagues, clients, or customers by [clicking here](#).

Permission to republish or repurpose articles or portions of articles can be obtained by following the guidelines [here](#).

The following resources related to this article are available online at www.sciencemag.org (this information is current as of May 31, 2015):

Updated information and services, including high-resolution figures, can be found in the online version of this article at:

<http://www.sciencemag.org/content/315/5819/1719.full.html>

Supporting Online Material can be found at:

<http://www.sciencemag.org/content/suppl/2007/04/05/315.5819.1719.DC1.html>

This article **cites 24 articles**, 8 of which can be accessed free:

<http://www.sciencemag.org/content/315/5819/1719.full.html#ref-list-1>

This article has been **cited by** 53 article(s) on the ISI Web of Science

This article has been **cited by** 51 articles hosted by HighWire Press; see:

<http://www.sciencemag.org/content/315/5819/1719.full.html#related-urls>

This article appears in the following **subject collections**:

Neuroscience

<http://www.sciencemag.org/cgi/collection/neuroscience>